Minimizing the interface-driven losses in inverted perovskite solar cells and modules

Xin Zhang,[abcdef] Weiming Qiu,[*g] Sofia Apergi,[hi] Shivam Singh,[j] Paulo Marchezi, [j] Wenya Song,[cg] Christian Sternemann,[k] Karim Elkhouly,[cg] Dong Zhang,[l] Aranzazu Aguirre,[def] Tamara Merckx, [def] Anurag Krishna, [def] Yuanyuan Shi,[m] Andrea Bracesco,[n] Cristian van Helvoirt,[n] Frennie Bens,[o] Valerio Zardetto,[l] Jan D'Haen,[f] Anran Yu,[b] Geert Brocks,[hip] Tom Aernouts,[def] Ellen Moons,[j] Shuxia Tao,[hi] Yiqiang Zhan,[*ab] Yinghuan Kuang,[*def] and Jef Poortmans[cdef]

[a] Academy for Engineering & Technology (FAET), Fudan University, Handan 220, 200433 Shanghai, China

[b] Center for Micro Nano Systems, School of Information Science and Technology (SIST), Fudan University, Handan 220, 200433 Shanghai, China

[c] Department of Electrical Engineering (ESAT), KU Leuven, Kasteelpark Arenberg 10, 3001 Leuven, Belgium

[d] Imec, imo-imomec, Thin Film PV Technology – partner in Solliance, Thor Park 8320, 3600 Genk, Belgium

[e] EnergyVille, imo-imomec, Thor Park 8320, 3600 Genk, Belgium

[f] Hasselt University, imo-imomec, Martelarenlaan 42, 3500 Hasselt, Belgium

[g] imec - SAT department, Kapeldreef 75, 3001 Leuven, Belgium

[h] Materials Simulation and Modelling, Department of Applied Physics, Eindhoven University of Technology, 5600 MB Eindhoven, The Netherlands

[i] Center for Computational Energy Research, Department of Applied Physics, Eindhoven University of Technology, 5600 MB Eindhoven, The Netherlands

[j] Department of Engineering and Physics, Karlstad University, SE-651 88 Karlstad, Sweden

[k] Fakultät Physik/DELTA, Technische Universität Dortmund, Maria-Goeppert-Mayer-Straße 2, D-44227 Dortmund, Germany

[l] TNO, High Tech Campus 21, 5656 AE Eindhoven, The Netherlands

[m] School of Microelectronics, University of Science and Technology of China, Jinzhai 96, 230026 Hefei, China

[n] Department of Applied Physics and Science Education, Eindhoven University of Technology, 5600 MB Eindhoven, The Netherlands

[o] TNO, High Tech Campus 31, 5656 AE Eindhoven, The Netherlands

[p] Computational Materials Science, Faculty of Science and Technology and MESA+ Institute for Nanotechnology, University of Twente, 7500 AE Enschede, The Netherlands

Corresponding authors:

Email: Weiming.Qiu@imec.be, yqzhan@fudan.edu.cn, Yinghuan.Kuang@imec.be

Abstract

The inverted p-i-n perovskite solar cells (PSCs) hold high promise for upscaling toward commercialization. However, the interfaces between the perovskite and the charge transport layers contribute to major power conversion efficiency (PCE) loss and instability. Here, we use a single material of 2-thiopheneethylammonium chloride (TEACl) to molecularly engineer the interface between perovskite and fullerene-C_{60} electron transport layer (ETL), and the buried interface between perovskite and NiO_x based hole transport layer (HTL). The dual interface modification results in optimized band alignment, suppressed non-radiative recombination and improved interfacial contact. A PCE of 24.3% is demonstrated, with open-circuit voltage (V_{oc}) and fill factor (FF) of 1.17 V and 84.6% respectively. The unencapsulated device retains above 97.0% of the initial performance after 1000 h of maximum power point tracking under illumination. Moreover, a PCE of 22.6% and a remarkable FF of 82.4% are obtained for a mini-module with an active area of 3.63 cm^2.

Metal halide perovskites have emerged as highly promising candidates for photovoltaics with the certified PCEs reaching 25.8% and 33.2% for single junction and perovskite/silicon (Si) tandem solar cells, respectively.[1] Despite the high efficiencies, industrial compatible processing techniques, large-area film homogeneity, and long-term stability, need to be secured towards the commercialization of PSCs. To date, most of the reported highly efficient PSCs were obtained based on the regular n-i-p architecture.[2-7] Inverted p-i-n PSCs are gradually gaining more attention since they are generally more stable and can employ low-cost transport materials such as inorganic nickel oxides (NiO_x) as the HTL,[8-12] and fullerenes as the ETL.[13] Additionally, these cost-effective transport materials can be processed with large-scale industrially compatible deposition techniques such as sputtering and thermal evaporation, which makes them ideal for upscaling toward industrialization. Moreover, the PCE of inverted PSCs is approaching that of the regular n-i-p PSCs.[7,14-16]

It has been widely reported that the interfaces between the perovskite and the charge transport layers contribute to the majority of PCE losses and instability in these inverted devices. Consequently, enormous efforts have been taken on the development of new strategies to mitigate interface-driven losses and instabilities. For instance, modifying the buried HTL/perovskite interface has been proven effective in enhancing the device performance and stability, by improving the energy level alignment, regulating the perovskite crystallization, and reducing interfacial defects.[17-19] On the other hand, the upper perovskite interface with the ETL has generally been neglected due to that the fullerene ETL is expected to passivate the

perovskite surface defects.[20,21] However, it has been revealed that only weak interactions are created between fullerene derivatives and perovskite.[22] In addition, a flawed contact between the perovskite surface and C_{60} molecules may induce deep-level defects, thus hindering the device performance.[23,24] Therefore, modifying the perovskite upper interface is critically important. Recently it has been shown that by constructing heterojunctions or functionalizing the upper interface with organometallic compounds, both device efficiency and operational stability can be significantly improved.[22,25,26] However, very few studies have simultaneously engineered both HTL/perovskite and perovskite/ETL interfaces with one single material in inverted PSCs.[27]

In this work, we report a dual interface engineering strategy passivating deleterious defects and optimization of the band alignment in inverted PSCs. We use ammonium salt namely TEACl for this dual passivation. Previously, TEACl has been introduced to the perovskite upper surface to form 2D/3D perovskite heterojunction,[28] react with the excess PbI_2 to improve the light-stability and passivate surface defects for higher photovoltage.[29-31] However, these studies only focused on a single interface, demonstrated PSCs with relatively lower PCEs, and had limited mechanistic investigations. To maximize performance gains, besides the perovskite top surface, in this work TEACl is also been applied to the buried HTL/perovskite interface. To gain insights into the origins of performance enhancement we perform in-depth structural and optoelectronic characterizations along with molecular dynamics and density functional theory (DFT) calculations. Owing to the dual interface modifications, we passivate the deleterious defects, optimize the band alignment, and improve the interfacial contact. A PCE of 24.3% is therefore obtained for the inverted PSC built on NiO_x based HTL. The unencapsulated device exhibits extraordinary operational stability with remaining above 97% of its initial performance after 1000 hours of maximum power point tracking under simulated continuous 1-Sun illumination at 60 °C in N_2. Excellent thermal stability at 85 °C is also demonstrated, with about 88% retained after ~1850 hours of aging under N_2 atmosphere. It is worth to note that to date most of the high-performance PSCs are processed using the antisolvent approach for perovskite deposition.[16,22,25,26] While in this work we use a scalable, cost-effective and environmentally friendly N_2 gas quenching with great potential for upscaling.[32] With this dual interface optimization strategy, reproducible perovskite mini-modules can be obtained with a maximum PCE of 22.6% and a remarkably high FF of 82.4% on an active area of 3.63 cm^2. In addition, dual interface modulations have been proven beneficial for various perovskite compositions deposited by different processing methods on

different HTLs, indicating their effectiveness for different perovskite compositions and device stacks.

Device Performance and Stability

In this work, we conduct the study based on the device architecture of MgF_2/glass/ITO/NiO_x/Me-4PACz/(TEACl)/perovskite/(TEACl)/LiF/C_{60}/BCP/Cu (**Figure 1a**). In the device, MgF_2 is used as an antireflection coating layer, ITO is indium tin oxide, NiO_x stands for nickel oxide nanoparticles, Me-4PACz is [4-(3,6-Dimethyl-9H-carbazol-9-yl)butyl]phosphonic acid, LiF is lithium fluoride, BCP is bathocuproine, and the perovskite nominal composition is $Cs_{0.1}FA_{0.9}PbI_{2.855}Br_{0.145}$, which is prepared by gas-quenching technique according to our previous work.[26] The cross-sectional scanning electron microscopy (SEM) image of the perovskite layer indicates that the film thickness is about 500 nm (**Figure S1**). We find that the combination of NiO_x and Me-4PACz, which serves as the baseline bi-layer HTL in this work, enables highly reproducible and efficient gas-quenched PSCs (**Figure S2**), which is in agreement with what was previously reported in the literature with atomic layer deposited (ALD)-NiO_x/SAM.[33] A two-step interface modification strategy is employed, where the perovskite surface is subjected to TEACl treatment, denoted as Upper in the manuscript. This step aims to passivate the surface defects and improve the interfacial contact between the perovskite and C_{60}. In conjunction with the upper interface, TEACl is also introduced to the buried HTL/perovskite interface, denoted as Dual in the following text. The concentrations of TEACl used in this work are 1.0 mg/mL, which is determined based on a screening experiment (**Figure S3**). The PSC without TEACl modifications is denoted as Control.

We first study the device performance of the PSCs based on these interface modification conditions. **Figure 1b** shows the current density-voltage (*J-V*) curves of the best devices. The Control device shows a PCE of 22.4% with short-circuit current density (J_{sc}), V_{oc} and FF of 24.1 mA/cm^2, 1.13 V, and 82.3%, respectively. In the Upper case, J_{sc}, $V_{oc,}$ and FF slightly increase to 24.3 mA/cm^2, 1.16 V, and 83.0%, respectively, resulting in a PCE of 23.4%. When both interfaces are treated (i.e., Dual case), the photovoltaic parameters are enhanced to 24.5 mA/cm^2, 1.17 V, and 84.6%, resulting in a champion PCE of 24.3%. Maximum power point tracking (MPPT) PCEs are recorded during 10 minutes by a dynamic tracking algorithm based on our previous study.[34] As shown in the inset of **Figure 1b**, the Control, Upper and Dual devices show stabilized PCEs of 22.1%, 22.8%, and 23.5%, respectively. The corresponding external quantum efficiency (EQE) spectra and the integrated J_{sc}, as given in **Figure S4**, agree well with the J_{sc} from *J-V* curves, i.e., less than 3% discrepancy in all cases. The variation of PV parameters of the corresponding PSCs from different batches are shown

in **Figure S5**, demonstrating excellent reproducibility of the developed processes. The detailed results are summarized in **Table S2**. Evidently, the average J_{sc} shows comparable values for different treatments, while V_{oc} and FF are the main contributors to the enhanced device performance. The average PCE increases from 21.5% for the Control devices to 22.4% for the Upper devices, and further to 23.4% for the Dual devices. In addition, all devices show only minor hysteresis, with a hysteresis index of less than 4% (**Figure S6**).

Next, we fabricate perovskite mini-modules with an aperture area of 4 cm^2. The mini-module has the classic P1, P2, and P3 scribes by picosecond laser scribing, generating a geometrical fill factor (GFF) of 90.8% (see **Figure S7**) and thus resulting in an active area of 3.63 cm^2. **Figure 1c** shows the *J-V* curve of the best module, which has an active area PCE of 22.6% (aperture area efficiency of 20.5%), with J_{sc}, $V_{oc,}$ and FF of 5.93 mA/cm^2, 4.63 V, and 82.4%, respectively. Each sub-cell in the mini-module has a V_{oc} of ~1.16 V, which is close to the V_{oc} obtained from the small-scale PSCs, indicating excellent homogeneity of perovskite absorber and interfaces over the entire module area. The perovskite mini-module shows a stable output with a PCE of 22.0% during the 10-min MPPT measurement (**Figure S8**). **Figure S9** shows the active area PCE distribution of 7 mini-modules with the Dual modification. All the devices show PCEs exceeding 21.5% with an average PCE of 22.0%, demonstrating excellent module reproducibility. Similar to the small-size PSCs, the perovskite mini-modules also exhibit only small hysteresis of 2.3% (**Figure S10**).

Long-term stability is one of the key weaknesses of PSCs. We investigate the operational and thermal stability of the PSCs with respect to ISOS L-2I and ISOS D-2I protocols respectively.[35] In PSCs, apart from the active layer and interfaces, unstable charge transport layers and buffer layers such as BCP can also affect the stability.[36] In addition, the migration of metal ions from the metal electrode to the perovskite layer can lead to failure.[37] To elude these potential issues while focusing on the intrinsic stability of the perovskite and its adjacent interfaces, BCP and Cu metal electrode are replaced by the more stable ALD SnO_2, and sputtered ITO as the electrode, respectively. The device performance of the semitransparent PSCs is presented in **Figure S11**. The long-term thermal stability is assessed by aging the PSCs at 85 °C in dark conditions under N_2 atmosphere. As shown in **Figure 1d**, the Dual devices exhibit excellent thermal stability, i.e. retaining about 88% of its initial performance after ~1850 hours of aging. While the PSCs without any treatment retain only 55% of the initial performance. The dual interfacial TEACl treatments help to suppress J_{sc} and FF losses (**Figure S12**). Fresh Dual cells with the proven thermal stability of the cell stack were selected for even harsher stability test, i.e., the long-term operational stability test at MPPT

condition under simulated 1-Sun continuous illumination at a temperature of 60 °C for 1000 h.[38] As shown in **Figure 1e**, the Dual device shows excellent stability with above 97% of its initial performance maintained. To put our performance and stability results in perspective, we summarize the best PCE and long-term operational stability of p-i-n based PSCs from the literature in **Figure S13**, **Table S1**, which shows that our target PSC compares favorably with other reported results.

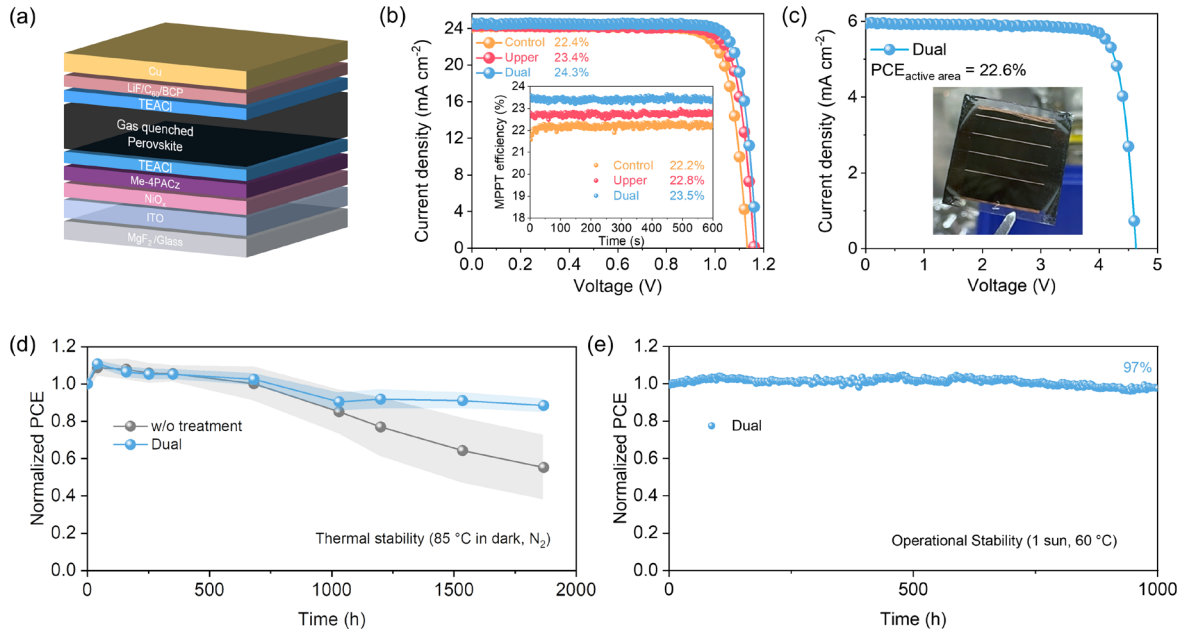

Figure 1 Device performance and stability of the gas-quenched inverted PSCs. (a) Schematic diagram of the device architecture. (b) *J-V* curves of the best-performing devices for each interface modification condition. Inset shows the corresponding 10 min-MPPT measurements at 30 °C in an N_2-filled glove box. (c) *J-V* curve of the best-performing perovskite mini-module, with the inset showing a photograph of the mini-module on glass substrate side. Long-term stability measurements of the unencapsulated PSCs with the Dual treatments: (d) Normalized PCE evolution aged at 85 °C in dark conditions in N_2 atmosphere. The shaded area indicates the standard deviation of 10 devices. The device architecture is glass/ITO/NiO_x/Me-4PACz/TEACl/perovskite/TEACl/C_{60}/temporal ALD SnO_2/ITO. (e) The operational stability at 60 °C under simulated continuous 1-Sun illumination in N_2 atmosphere. The device architecture is glass/ITO/NiO_x/Me-4PACz/TEACl/perovskite/TEACl/C_{60}/spatial ALD SnO_2/ITO.

Optoelectronic Properties and Charge Carrier Recombination

It is well known that V_{oc} is strongly associated with defects present in the perovskite bulk and at the interfaces. In this regard, we first perform time-resolved photoluminescence (TRPL) measurements for the perovskite films on glass/ITO/NiO_x/Me-4PACz substrates (**Figure 2a**). After fitting the data with a bi-exponential function, the calculated average carrier lifetime of the Control film is 614 ns, which is improved to 889 ns and 1109 ns for the Upper and the Dual cases, respectively (**Table S3**). In addition, we perform transient photo-voltage

(TPV) decay measurements to evaluate the carrier lifetime in the operating devices. As displayed in **Figure 2b**, the carrier lifetime is improved from 8.9 μs for the Control device to 13.2 μs and further to 17.5 μs for the Upper and the Dual devices, respectively. The extended carrier lifetimes in TRPL and TPV imply the reduction of non-radiative recombination possibly due to the passivation of trap states, which is beneficial for enhancing the V_{oc}.[39-41]

Next, in order to obtain the ideality factor, the *J-V* curves of sputtered NiO_x based PSCs are measured in dark conditions and further fitted based on the single diode model. As shown in **Figure S14a**, the ideality factor for the Control device is 1.82, which is reduced to 1.58 for the Upper device and further to 1.37 for the Dual device. The decreased ideality factor indicates that trap-assisted recombination is suppressed. In addition, we carry out the pulsed space-charge-limited current measurements on the hole-only devices, using the pulse length of 100 ms. As shown in **Figure S14b**, the trap-filled-limited voltage (V_{TFL}) for the corresponding devices are 1.18 V, 0.80 V and 0.63 V, respectively. The trap state density (N_t) can be determined based on the equation of $N_t = 2\varepsilon_0\varepsilon_r V_{TFL}/qL^2$,[26] where ε_0 is the vacuum permittivity, ε_r represents perovskite dielectric constant, q is the elementary charge and L is the thickness of the perovskite film. It is found that the trap state density of the Control device is 2.45×10^{16} cm^{-3}, which decreases to 1.66×10^{16} cm^{-3} after the upper TEACl modification. Under the dual interface modification, the trap state density exhibits the lowest value of 1.31×10^{16} cm^{-3}. These results suggest that the defects can be effectively passivated by the TEACl modification.

To further understand the defect passivation effect, a quantitative analysis of V_{oc} loss is conducted for the corresponding PSCs according to the detailed balance theory.[18,26,42] Details of this theory can be found in the Supporting Information (i.e., Equations S3-S15). The V_{oc} loss mainly has 3 components viz. ΔV_1, which is due to the radiative recombination involving energies above the perovskite band gap E_g; ΔV_2, which is the blackbody radiation-induced energy loss; ΔV_3, which represents the non-radiative recombination loss. The first component of V_{oc} loss (ΔV_1) is around 283 mV for all the three cases. We conduct highly sensitive EQE measurements for the PSCs as shown in **Figure 2c**, from which we establish the second component of V_{oc} loss (ΔV_2) to be around 10 mV for all the devices under different conditions. These negligible changes in the first two components imply that the interface treatment mainly passivates the non-radiative recombination centers (ΔV_3). This is corroborated by the EQE of electroluminescence (EQE_{EL}). Indeed, as seen in **Figure 2d**, the EQE_{EL} values at 1-Sun equivalent current injection are found to be 0.63%, 1.55%, and 1.82% for the Control, the Upper, and the Dual devices respectively. Therefore, ΔV_3 of the Control device is 131 mV.

When the interface modifications are applied, it is reduced to 108 mV for the Upper device and 104 mV for the Dual device. The values of the three components are displayed in **Figure 2e** and summarized in **Table S4**. Interestingly, a reduction of 23 mV in ΔV_3 is observed with Upper modification, while it is only further reduced by 4 mV with Dual modification. It demonstrates that surface passivation to prevent non-radiative recombination induced V_{oc} reduction is most effective at the perovskite/ETL interface.

Next, we conduct quasi-Fermi level splitting (QFLS) measurements for the half-completed device stack of glass/ITO/NiO_x/Me-4PACz/(TEACl)/perovskite/(TEACl). As shown in **Figure 2f** and **Figure S15**, all the perovskite films exhibit similar QFLS values of around 1.18 eV, with differences of less than 7 meV between each. However, the average V_{oc} measured from *J-V* scans (**Figure S5**) for the Control devices is ~50 mV lower (i.e., 1.13 V), which we believe is due to the loss after the deposition of ETLs. This loss is reduced to ~20 mV (i.e., average V_{oc} of 1.16 V) with the Upper modification. The additional buried interface modification further contributes to a ~10 mV loss reduction. Furthermore, the QFLS value obtained on the completed devices is ~1.15 eV, which matches well with the measured device V_{oc} from *J-V* scan (**Figure S16**). These results are consistent with the quantitative V_{oc} loss analysis and confirm that the enhanced V_{oc} in the complete devices is mainly due to the improved perovskite/ETL interface.

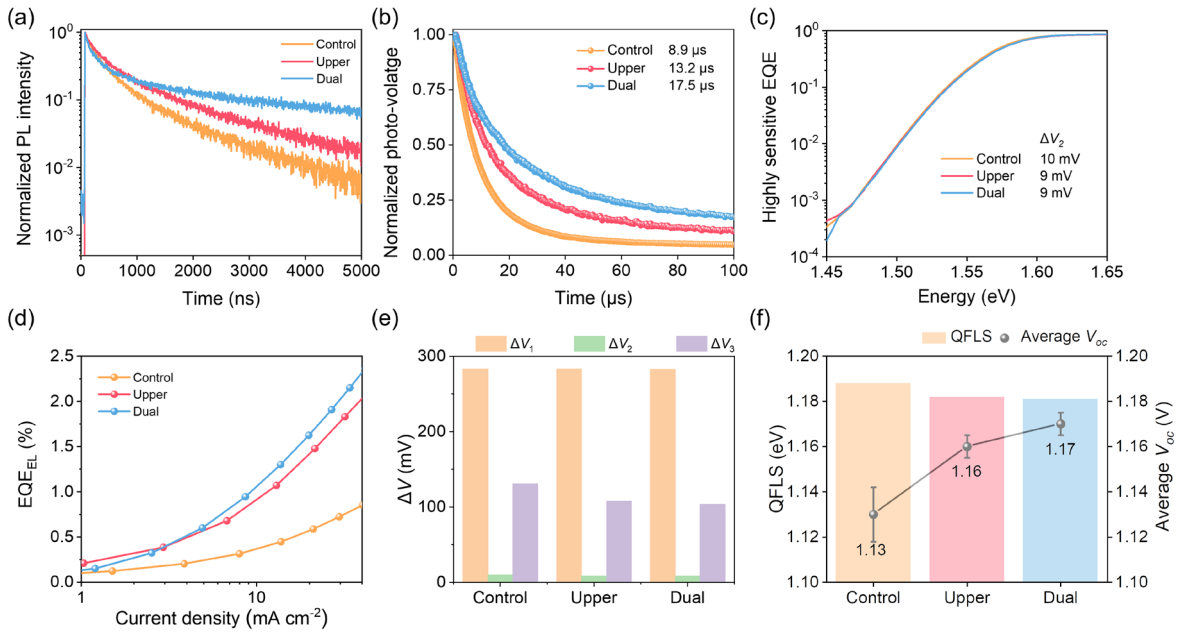

Figure 2 Defect passivation analysis. (a) TRPL spectra of the perovskite films based on different interface modification conditions. (b) TPV measurements, (c) highly sensitive EQE, and (d) EQE_{EL} of the corresponding PSCs. (e) Overall V_{oc} loss analysis based on the detailed balance theory. (f) Comparison of the QFLS values (the columns) for half-completed devices (up to the perovskite layer with surface treatments) with the measured average V_{oc} of completed cells (the spheres).

Structural, Morphological and Interfacial Analysis

We carry out detailed investigations to understand the impact of the dual interface treatment on the structural, morphological, and interfacial properties of the perovskite. The optical absorption and crystal structure of the perovskite films are acquired by UV-Vis spectrophotometer and XRD, respectively. All the perovskite films demonstrate similar absorption spectra with a cutoff at around 790 nm (**Figure S17a**). From the XRD patterns, all the films show the same main diffraction peaks located at 14.0° and 28.2°, corresponding to the (001) and (002) planes of cubic-phase perovskite (**Figure S17b**).[43] The full width at half maximum (FWHM) values of the (001) plane for all conditions are ~0.17° (**Figure S17c**). These results indicate that the perovskite bulk structural properties remain identical after the dual interface treatments. Therefore, we believe that the device performance enhancement is not related to any change in bulk quality, but rather to the modulation of the interfaces. Morphological inspections are performed via SEM. Top-view SEM images (**Figure 3a**) of all the samples show a compact morphology with grain sizes ranging from hundreds of nanometers to a few microns. The average grain size of all conditions is ~ 700 nm (**Figure S17d)**. However, in the Upper and Dual samples, tiny flake-like structures appear on the perovskite grain surface. This is verified by AFM images as shown in **Figure 3b**, while from the AFM images acquired in tapping mode, it is evidenced that these structures spread over the entire surface of the film (**Figure S18**). With the TEACl treatment, the root mean square (RMS) roughness (*R*q) of the films is reduced by 2-3 nm.

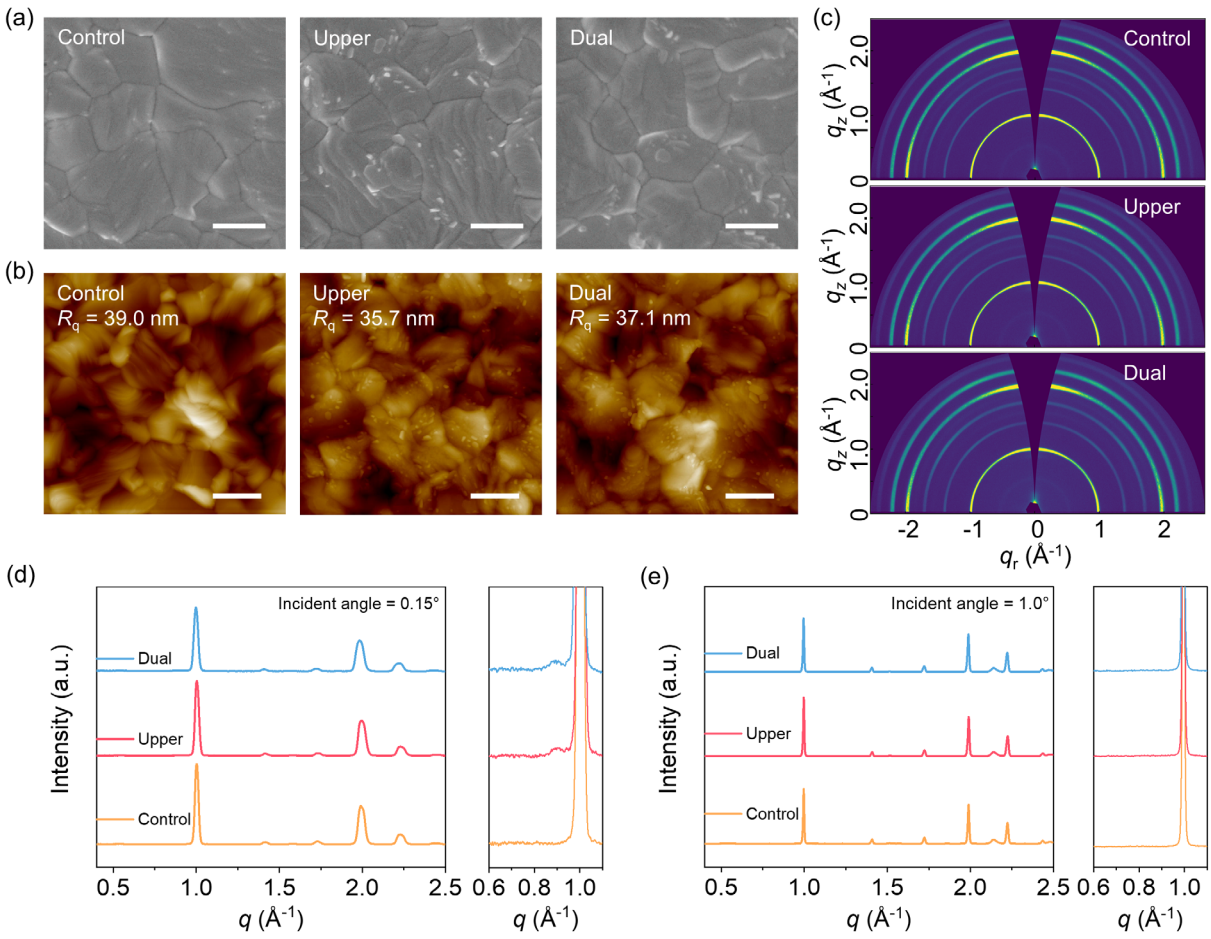

Figure 3 Analysis of the morphological and structural properties. (a) Top-view SEM images with scale bars of 500 nm, (b) AFM topography images with scale bars of 1 μm, and (c) 2D GIWAXS patterns of the perovskite films under different interface treatment conditions. The extracted out-of-plane profiles with an incident angle of (d) 0.15°, and (e) 1.0°. A zoomed-in view in the range of 0.6 Å^{-1} - 1.1 Å^{-1} is also shown on the right for each incident angle. The y-axis scale for the two zoomed-in graphs is the same.

Figure 3c shows the 2D GIWAXS patterns of the corresponding films at 0.15° angle of incidence, and the extracted out-of-plane diffraction profiles are given in **Figure 3d**. It can be seen that all the films exhibit the same diffraction ring positions located at around 1 Å^{-1} and 2 Å^{-1}. However, when zoomed-in at around 0.9 Å^{-1}, an additional peak located close to the perovskite main peak appears for the TEACl-treated films, which should be assigned to the tiny flake-like structures observed by SEM and AFM measurements. These structures are found to be ultrathin on the perovskite surface, as there is no difference between the spectra when the higher incident angle of 1.0° is used (**Figure 3e**). In addition, low dimensional perovskite phases are not detected from the grazing incidence XRD (GIXRD) patterns, which remain almost the same for the Control and the Dual perovskites (**Figure S19**). Extra diffraction peaks located at smaller 2-theta degrees only appear at higher TEACl concentrations. Despite the

efforts, at this stage it is still uncertain to us what exactly these tiny structures are. Further investigations on this aspect are therefore currently ongoing. Nevertheless, the structural and morphological analysis hint toward the formation of an ultra-thin passivation layer without significant change in the bulk properties of the perovskite film.

To further investigate the surface properties, X-ray photoelectron spectroscopy (XPS) measurements are performed. As shown in **Figure 4a**, the C1s core level spectra of the Control device consist of three main peaks located at 288.1 eV, 286.3 eV, and 284.8 eV, which can be attributed to the $C{=}NH_2$, $C\text{-}NH_2$, and C-C/C-H bonds respectively.[44] In **Figure 4b** and **c**, after the TEACl treatment, the $C{=}NH_2$ and C-C peak positions remain unchanged, whereas the $C\text{-}NH_2$ peak shows an enhanced peak intensity, and its position shifts by ~0.3 eV in the Dual condition to a lower binding energy position, which can be contributed by the C-S bonds from TEACl. This indicates that TEA^+ cations are introduced at the perovskite surface. The Pb4f core level spectra are also acquired as shown in **Figure 4d**. The characteristic $Pb4f_{5/2}$ and $Pb4f_{7/2}$ doublet for the Control perovskite film are located at 143.3 eV and 138.5 eV, respectively. With modification by TEACl, these peaks shift to lower binding energy. Such peak shift could be attributed to the hydrogen bond between the ammonium groups from TEA^+ cations and the I from PbI_6^{4-} octahedra, which results in the reduced Pb-I bond strength, shifting the Pb4f peaks and I3d peaks (**Figure S20**) to lower binding energies.[45]

The energy levels of the perovskite films and HTL layers under different treatments are studied further by ultraviolet photoelectron spectroscopy (UPS). The UPS spectra are shown in **Figure S21**, and the summarized energy level alignment diagram is given in **Figure 4e**. All the perovskite films show n-type character. With the TEACl treatment, the conduction band minimum (CBM) of the perovskite is shifted upwards, increasing the energy offset between the perovskite and C_{60} ETL from 0.04 eV to ~0.2 eV in the Dual case, and thus providing a suitable driving force for efficient electron extraction across this interface.[46,47] Notably, the slightly increased energy levels of the Dual film as compared to the Upper film might be attributed to the interfacial dipole by the buried TEACl treatment (**Figure S22**). As for the buried interface, the NiO_x HTL shows a valence band maximum (VBM) value of -5.00 eV, which shifts downwards to -5.20 eV with Me-4PACz modification. This is likely caused by the surface dipole layer introduced by ordered self-assembled monolayers (SAMs), which facilitates the hole extraction at the interface.[48-50] With the introduction of TEACl on top of HTL (NiO_x/Me-4PACz), the VBM moves further down to -5.35 eV, which matches better with the VBM of the perovskite, i.e. the energy offset of ~0.5 eV in the Cotnrol device is reduced to ~0.2 eV in the Dual device. This can also provide suitable driving force for efficient hole

extraction. It should be noted that such a ~0.2 eV energy offset has negligible impact on the QFLS, as observed before (**Figure 2f**), but it can enable efficient carrier transport.

In order to study the effect of the buried TEACl treatment on the perovskite, XRD, UV-Vis absorption, steady-state PL and TRPL are performed. It is found that the buried TEACl has negligible impact on the perovskite crystal structure and film absorbance (**Figure S23a,b**), while the lower steady-state PL intensity, and the faster decay in the TRPL spectra indicate that the TEACl treatment could facilitate the extraction of photogenerated holes from perovskite to HTL (**Figure S23c,d**). Moreover, as shown in **Figure S24**, the trap state density can be reduced from 2.97×10^{16} cm^{-3} to 1.95×10^{16} cm^{-3} after the buried TEACl modification, indicating that TEACl could also passivate the defects at the buried HTL/perovskite interface, which is consistent with the previous results (**Figure 2** and **Figure S14b**). Therefore, the facilitated charge extraction, reduced trap density and better energy level alignment at the buried HTL/perovskite interface contribute to the enhancement of the device performace (**Figure S25**), and these results further contribute to explaining the enhanced FF and V_{oc}, as observed in the *J-V* scans for the Dual devices. In addition to the improved energy level alignment at this interface, SAMs may passivate the NiO_x surface states,[33,49,51,52] thus reducing interface recombination. Also, with the presence of SAMs and TEACl, direct interaction of the perovskite precursor solution with NiO_x could be prevented, which otherwise might form an unfavorable interlayer that hinders hole extraction across the perovskite/HTL interface.[10]

Density functional theory (DFT) calculations are conducted to further understand the role of TEACl treatment. As can be seen in **Figure 4f**, the organic cation, which consists of a thiophene ring, a short alkyl chain and an amine tail, adsorbs on the surface of the PbI_2-terminated perovskite, with the amine tail forming hydrogen bonds with the surface halides. Due to this interaction, amines are effective for the passivation of perovskite surfaces by reducing the density and/or migration of surface defects.[53] It is worth noting that in all the Control, Upper, and Dual devices, FACl is always used to first treat the perovskite surface. For the latter two cases, TEACl was further applied after the FACl treatment. The calculated adsorption energy (E_{ads}) of TEACl on the perovskite is much higher than that of FACl (-1.87 eV vs. -1.41 eV), indicating that TEACl can either readily adsorb on a PbI_2-terminated surface or replace FA on a FACl-terminated surface, in both cases leading to an overall more stable termination. Also important is that, unlike the FA cation, the bulkier TEA cation sticks out from the perovskite surface, allowing for the thiophene ring to better interact with C_{60}. Consequently, C_{60} adsorbs more strongly on the TEA passivated surface via van der Waals

interaction (i.e., the Upper and the Dual devices), with E_{ads} = -1.02 eV, than on the FACl terminated surface (i.e., the Control device), with E_{ads} = -0.75 eV.

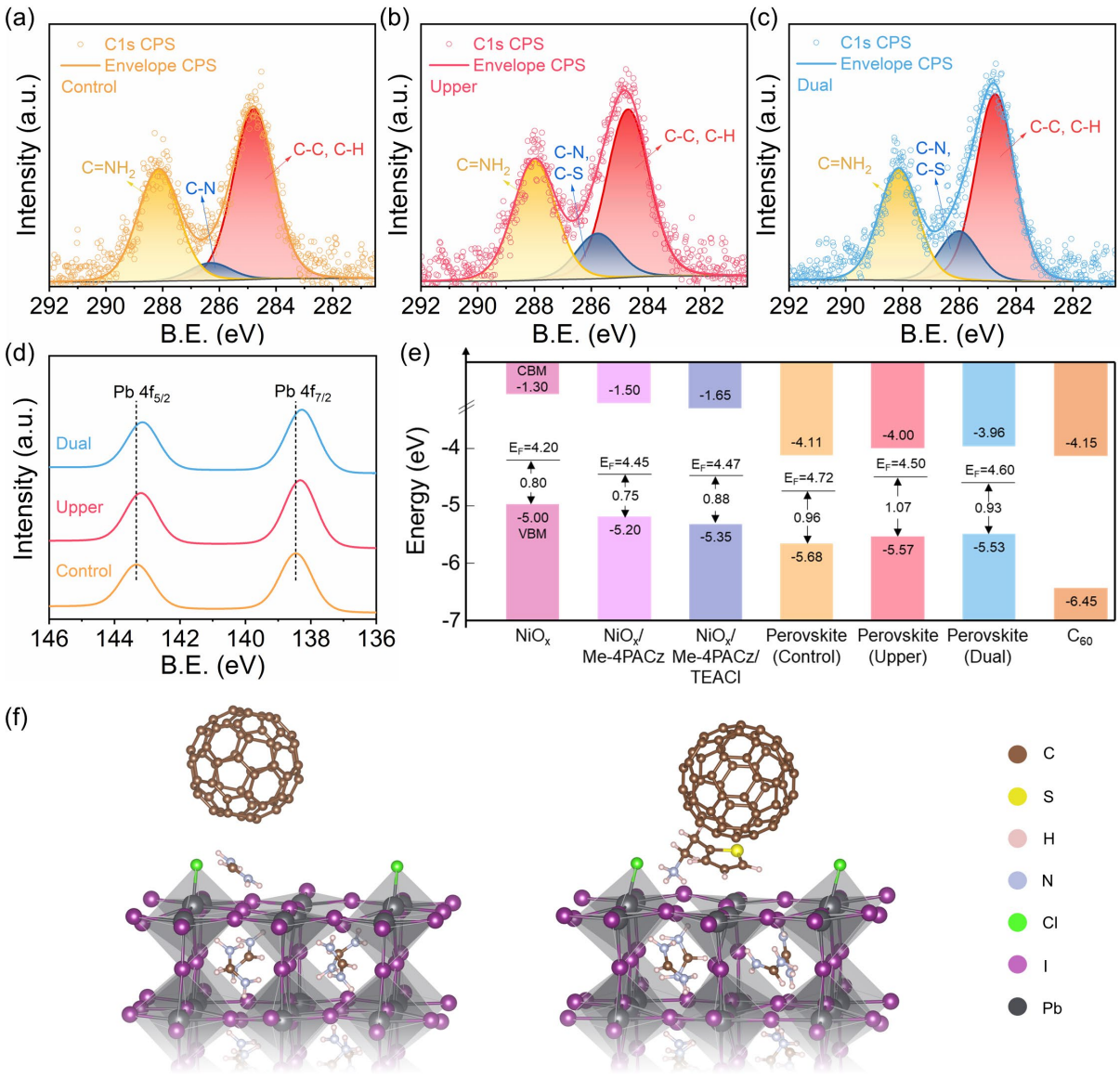

Figure 4 Surface properties of the perovskite films. C1s XPS spectra of the perovskite films based on (a) Control, (b) Upper, and (c) Dual conditions. CPS: counts per second. (d) Pb4f XPS spectra of the corresponding perovskite films. B.E.: binding energy; K.E.: kinetic energy. (e) Energy levels of the HTLs (NiO_x, NiO_x/4PACz, and NiO_x/4PACz/TEACl), the perovskite films with and without TEACl modifications, and the C_{60} ETL. (f) Density functional theory (DFT) calculations of the interactions of FACl (left) and TEACl (right) with perovskite and C_{60}.

TEACl passivation also modifies the electronic energy level alignment of the applied layers. When an ion pair is adsorbed on the surface of a material, the dipole moment of the former modifies the VBM position of the latter.[54] According to our DFT calculations, when TEACl is adsorbed on a PbI_2-terminated perovskite surface, it shifts its VBM 0.77 eV closer

to the vacuum level. This result, while larger in quantity, agrees qualitatively with the experimental findings by UPS (**Figure 4e**). The favorable shift caused by TEACl is much larger than the shift of 0.44 eV caused by FACl. Therefore, TEACl leads to a better electronic level alignment at the perovskite/ETL interface. The opposite effect can be expected for the buried HTL/perovskite interface. The thiophene group of the TEA molecule prefers to interact with the SAMs molecules, facilitated by the van der Waals interactions between the two organic species, while the amine group at the other end of the TEA molecule interacts with the perovskite, as do the Cl ions. Thus, the absolute orientation of TEACl pair, and hence the dipole moment, is the opposite of that on the top interface. The direction of the dipole moment at the buried interface is pointing towards the HTL, which will induce a similar effect on the energy level as the case of using SAMs to modify NiO_x HTL, making the VBM of NiO_x/Me-4PACz downshifts. This agrees with the results characterized by UPS. As a result, a better energy level alignment at the HTL/perovskite interface is also realized with TEACl modification.

While the superiority of TEA over FA is apparent, for the sake of comparison the same calculations have also been conducted for phenethylammonium (PEA) halide, one of the widely applied molecules for the chemical passivation of perovskites surface.[27,53,55-59] As can be seen in **Table S5**, the adsorption energies of the TEA and PEA on the surface of the perovskite are found to be very similar, which may be expected, since both molecules share the same amine tail. However, differences in geometry lead to both the adsorption energy of C_{60} and the VBM shift being higher for TEA, making TEA more advantageous than PEA as a surface modifier. Finally, replacing TEA-Cl with TEA-I leads to slightly a higher adsorption energy, but a smaller VBM shift. Since both adsorption energies are already quite high, the higher VBM shift of TEACl the decisive factor in this perovskite surface treatment.

Effectiveness of the Developed Interface Modification Strategy

In order to check the effectiveness of the Dual passivation approach, it is tested further on different perovskite compositions and layer stack. For instance, PSCs are fabricated with $Cs_{0.1}FA_{0.9}PbI_3$ as the photoactive layer obtained by spin-coating. The statistical distribution of photovoltaic parameters is shown in **Figure S26a-d** and is summarized in **Table S6**. Both V_{oc} and FF are greatly improved, resulting in an absolute average PCE gain of 3.0%, i.e., from 17.8% to 20.8%. The PCE of the best devices is boosted from 18.7% to 21.9% after the Dual modifications (**Figure S26e**). These devices show a small hysteresis and a stable MPPT PCE (**Figure S26f**,**g**).

To broaden the application scenario of the dual interface modification strategy, we have also prepared gas-quenched inverted PSCs using sputtered NiO_x as a replacement of NiO_x nanoparticles, since sputtered NiO_x holds greater potential for upscaling to large-scale manufacturing. The photovoltaic parameters are displayed in **Figure S27a-d** and summarized in **Table S7**. Upon the Dual treatments a significant increase in V_{oc} from 1.10 V to 1.16 V is obtained, contributing to the average PCE increasing from 20.0% to 21.8%. The champion device demonstrates a PCE of 23.0% with J_{sc}, $V_{oc,}$ and FF of 24.4 mA/cm^2, 1.16 V, and 81.3%, respectively, whereas the best control device shows a PCE of 21.3% (**Figure S27e**). The sputtered NiO_x-based devices exhibit noticeable hysteresis (**Figure S27f**), which manifests itself in the FF, and may stem from the low conductivity of the sputtered NiO_x. The Dual device shows a more stable MPPT PCE than the Control device (**Figure S27g**). In addition, a sputtered NiO_x-based perovskite mini-module of 4 cm^2 (active area 3.78 cm^2, GFF=94.5%) with the Dual modifications was also prepared, with J_{sc}, $V_{oc,}$ and FF of 5.85 mA/cm^2, 4.55 V, and 81.7% respectively, and a remarkable active area PCE of 21.7% (aperture area PCE of 20.5%, **Figure S28a**). A stable output of 20.9% during the 10-min MPPT measurement is obtained (**Figure S28b**). Finally, the Upper modification strategy is applied to mini-modules fabricated with blade-coated $Cs_{0.2}FA_{0.8}Pb(I_{0.947}Br_{0.053})_3$ perovskite on sputtered NiO_x. Here again, our TEACl based perovskite/C_{60} upper interface treatment improves the active area PCE of a mini-module from 16.2% to 17.8% (**Figure S29**). Overall, these results indicate that our interface engineering strategy can be applied to a variety of perovskite compositions and device stacks.

To summarize, in this work we demonstrated a unique strategy that employs a single molecule of TEACl for dual perovskite interface engineering. Consequently, PCEs of 24.3% and 22.6% are achieved for gas-quenched inverted perovskite solar cells and mini-modules, respectively. The unencapsulated device with TEACl-based dual interface modifications exhibits extraordinary operational and thermal stability. We found that most defects that contribute to non-radiative recombination centers are located at the perovskite/C_{60} interface, which can be effectively passivated by the TEACl treatment. In addition, the TEACl treatments at both interfaces improve the energy level alignment with suitable energy offsets, which act as the driving force for efficient charge extraction. DFT calculations reveal that the TEACl-modified interface is more stable and can strengthen the interaction between the perovskite and the C_{60} ETL. In addition, the adsorbed TEACl on the perovskite surface induces the upshift of the valence band maximum in the perovskite, which corroborates the experimental findings. Importantly, we confirm that the modification strategy is universal for devices composed of various perovskite compositions and HTLs in inverted PSCs and mini-modules. Our work

offers new insights to guide the development of highly efficient and stable perovskite cells and modules, thus paving the way to the scale-up and commercialization of perovskite PV.

Supporting information

Experimental details, theoretical calculations, Figures S1–S30 and Tables S1–S7 as mentioned in the text.

Author Contributions

X.Z. and W.Q. conceived the idea. X.Z. fabricated the devices, performed the characterizations of film property and device performance, conducted the V_{oc} loss analysis. X.Z. and W.Q. synthesized NiO_x NPs and performed the PL and TRPL measurements. Y.K. developed sputtered NiO_x, thermal evaporation processes of LiF, C_{60}, BCP, soft sputtering process of ITO atop perovskite stack, and daily supervised the work. S.A., G.B. and S.T. conducted the DFT calculations, S.A. wrote the DFT analysis in the manuscript. X.Z. and W.S. performed SEM and MPPT measurements. P.M., S.S. and E.M. conducted XPS and UPS measurements. C.S. conducted the GIWAXS measurement. K.E. performed EQE_{EL} measurement. D.Z. conducted the QFLS measurements. T.M. fabricated the blade-coated perovskite minimodules. A.A. performed laser scribing for the interconnection of the mini-modules. C.H. performed the GIXRD measurements. Y.S. performed the AFM measurement. A.B. prepared the temporal ALD SnO_2. B.F. and V.Z. prepared the spatial ALD SnO_2. J.D. performed XRD and cross-sectional SEM measurements. X.Z. wrote the manuscript and first revised by A.K. and Y.K. The project was supervised by W.Q., Y.K., Y.Z. and J.P. All authors contributed to the manuscript review and scientific discussions.

Conflicts of interest

The authors declare no conflict of interest.

Acknowledgements

X.Z., Y.K., and T.A. acknowledge the funding from the European Union's Horizon 2020 research and innovation program under grant agreement No. 850937 of the PERCISTAND project. Y.K., T.A., P.M., S.S., and E.M. acknowledge the funding from the FLAG-ERA JTC 2019 programme under Reference Number of JTC-2019-013 of the LASERGRAPH project. A.K. and T.A. acknowledge the FWO for the funding of the SBO project PROCEED (S002019N). This work is funded in part by the Kuwait Foundation for the Advancement of

Sciences under project numbers CN18-15EE-01 and PN1734SC02. Y.Z. acknowledges the funding from the National Natural Science Foundation of China under the grant number of 62274040. S.T. and S.A. acknowledge funding by the NWO START-UP support from The Netherlands. C.S. acknowledges DELTA (TU Dortmund, Germany) for providing synchrotron radiation at beamline BL9. Moreover, K.E. acknowledges funding from the European Research Council under the European Horizon 2020 Programme/ERC grant agreement no. 835133 (ULTRA-LUX). We are grateful to Dr. Zafer Hawash for his contributions in the early stage of the project and Dr. Hanmin Zhang and Dr. Leif K.E. Ericsson at Karlstad University for their support with the X-ray photoelectron spectroscopy. X.Z. and Y.K. thank Dr. Nga Phung and Prof. Dr. Mariadriana Creatore at Eindhoven University of Technology for the fruitful discussion on ALD SnO_2 and GIXRD results. X.Z. would like to thank Dr. Huotian Zhang from Linköping University for the fruitful discussions regarding the V_{oc} loss analysis. C.S. would like to thank Prof. Hans-Georg Steinrück from Paderborn University and Prof. Michael Paulus from Technische Universität Dortmund for helpful discussions.

References

1. Best Research-Cell Efficiencies. *Best Research-Cell Efficiencies,* National Renewable Energy Laboratory, accessed on 4 May (2023), URL: https://www.nrel.gov/pv/cell-efficiency.html.
2. Min, H.; Lee, D. Y.; Kim, J.; Kim, G.; Lee, K. S.; Kim, J.; Paik, M. J.; Kim, Y. K.; Kim, K. S.; Kim, M. G.; Shin, T. J.; Il Seok, S., Perovskite solar cells with atomically coherent interlayers on SnO2 electrodes. *Nature* **2021**, *598* (7881), 444-450.
3. Kim, M.; Jeong, J.; Lu, H.; Lee, T. K.; Eickemeyer, F. T.; Liu, Y.; Choi, I. W.; Choi, S. J.; Jo, Y.; Kim, H.-B.; Mo, S.-I.; Kim, Y.-K.; Lee, H.; An, N. G.; Cho, S.; Tress, W. R.; Zakeeruddin, S. M.; Hagfeldt, A.; Kim, J. Y.; Grätzel, M.; Kim, D. S., Conformal quantum dot-SnO_2 layers as electron transporters for efficient perovskite solar cells. *Science* **2022**, *375* (6578), 302-306.
4. Sidhik, S.; Wang, Y.; De Siena, M.; Asadpour, R.; Torma, A. J.; Terlier, T.; Ho, K.; Li, W.; Puthirath, A. B.; Shuai, X.; Agrawal, A.; Traore, B.; Jones, M.; Giridharagopal, R.; Ajayan, P. M.; Strzalka, J.; Ginger, D. S.; Katan, C.; Alam, M. A.; Even, J.; Kanatzidis, M. G.; Mohite, A. D., Deterministic fabrication of 3D/2D perovskite bilayer stacks for durable and efficient solar cells. *Science* **2022**, *377* (6613), 1425-1430.
5. Zhang, F.; Park, S. Y.; Yao, C.; Lu, H.; Dunfield, S. P.; Xiao, C.; Uličná, S.; Zhao, X.; Du Hill, L.; Chen, X.; Wang, X.; Mundt, L. E.; Stone, K. H.; Schelhas, L. T.; Teeter, G.; Parkin, S.; Ratcliff, E. L.; Loo, Y.-L.; Berry, J. J.; Beard, M. C.; Yan, Y.; Larson, B. W.; Zhu, K., Metastable Dion-Jacobson 2D structure enables efficient and stable perovskite solar cells. *Science* **2022**, *375* (6576), 71-76.
6. Zhang, T.; Wang, F.; Kim, H.-B.; Choi, I.-W.; Wang, C.; Cho, E.; Konefal, R.; Puttisong, Y.; Terado, K.; Kobera, L.; Chen, M.; Yang, M.; Bai, S.; Yang, B.; Suo, J.; Yang, S.-C.; Liu, X.; Fu, F.; Yoshida, H.; Chen, W. M.; Brus, J.; Coropceanu, V.; Hagfeldt, A.; Brédas, J.-L.; Fahlman, M.; Kim, D. S.; Hu, Z.; Gao, F., Ion-modulated radical doping of spiro-

OMeTAD for more efficient and stable perovskite solar cells. *Science* **2022**, *377* (6605), 495-501.
7. Zhao, Y.; Ma, F.; Qu, Z.; Yu, S.; Shen, T.; Deng, H.-X.; Chu, X.; Peng, X.; Yuan, Y.; Zhang, X.; You, J., Inactive $(PbI_2)_2RbCl$ stabilizes perovskite films for efficient solar cells. *Science* **2022**, *377* (6605), 531-534.
8. Yin, X.; Guo, Y.; Xie, H.; Que, W.; Kong, L. B., Nickel Oxide as Efficient Hole Transport Materials for Perovskite Solar Cells. *Solar RRL* **2019**, *3*, 1900001.
9. Ma, F.; Zhao, Y.; Li, J.; Zhang, X.; Gu, H.; You, J., Nickel oxide for inverted structure perovskite solar cells. *Journal of Energy Chemistry* **2021**, *52*, 393-411.
10. Boyd, C. C.; Shallcross, R. C.; Moot, T.; Kerner, R.; Bertoluzzi, L.; Onno, A.; Kavadiya, S.; Chosy, C.; Wolf, E. J.; Werner, J.; Raiford, J. A.; de Paula, C.; Palmstrom, A. F.; Yu, Z. J.; Berry, J. J.; Bent, S. F.; Holman, Z. C.; Luther, J. M.; Ratcliff, E. L.; Armstrong, N. R.; McGehee, M. D., Overcoming Redox Reactions at Perovskite-Nickel Oxide Interfaces to Boost Voltages in Perovskite Solar Cells. *Joule* **2020**, *4* (8), 1759-1775.
11. Koushik, D.; Jošt, M.; Dučinskas, A.; Burgess, C.; Zardetto, V.; Weijtens, C.; Verheijen, M. A.; Kessels, W. M. M.; Albrecht, S.; Creatore, M., Plasma-assisted atomic layer deposition of nickel oxide as hole transport layer for hybrid perovskite solar cells. *Journal of Materials Chemistry C* **2019**, *7* (40), 12532-12543.
12. Du, M.; Zhao, S.; Duan, L.; Cao, Y.; Wang, H.; Sun, Y.; Wang, L.; Zhu, X.; Feng, J.; Liu, L.; Jiang, X.; Dong, Q.; Shi, Y.; Wang, K.; Liu, S., Surface redox engineering of vacuum-deposited NiOx for top-performance perovskite solar cells and modules. *Joule* **2022**, *6* (8), 1931-1943.
13. Li, B.; Zhang, W., Improving the stability of inverted perovskite solar cells towards commercialization. *Communications Materials* **2022**, *3*, 65.
14. Peng, W.; Mao, K.; Cai, F.; Meng, H.; Zhu, Z.; Li, T.; Yuan, S.; Xu, Z.; Feng, X.; Xu, J.; McGehee, M. D.; Xu, J., Reducing nonradiative recombination in perovskite solar cells with a porous insulator contact. *Science* **2023**, *379* (6633), 683-690.
15. Park, J.; Kim, J.; Yun, H.-S.; Paik, M. J.; Noh, E.; Mun, H. J.; Kim, M. G.; Shin, T. J.; Seok, S. Il., Controlled growth of perovskite layers with volatile alkylammonium chlorides. *Nature* **2023**, *616*, 724-730.
16. Jiang, Q.; Tong, J.; Xian, Y.; Kerner, R. A.; Dunfield, S. P.; Xiao, C.; Scheidt, R. A.; Kuciauskas, D.; Wang, X.; Hautzinger, M. P.; Tirawat, R.; Beard, M. C.; Fenning, D. P.; Berry, J. J.; Larson, B. W.; Yan, Y.; Zhu, K., Surface reaction for efficient and stable inverted perovskite solar cells. *Nature* **2022**, *611* (7935), 278-283.
17. Gao, Z. W.; Wang, Y.; Choy, W. C. H., Buried Interface Modification in Perovskite Solar Cells: A Materials Perspective. *Advanced Energy Materials* **2022**, *12*, 2104030 .
18. Wu, S.; Zhang, J.; Li, Z.; Liu, D.; Qin, M.; Cheung, S. H.; Lu, X.; Lei, D.; So, S. K.; Zhu, Z.; Jen, A. K. Y., Modulation of Defects and Interfaces through Alkylammonium Interlayer for Efficient Inverted Perovskite Solar Cells. *Joule* **2020**, *4* (6), 1248-1262.
19. Li, J.; Zuo, L.; Wu, H.; Niu, B.; Shan, S.; Wu, G.; Chen, H., Universal Bottom Contact Modification with Diverse 2D Spacers for High-Performance Inverted Perovskite Solar Cells. *Advanced Functional Materials* **2021**, *31*, 2104036.
20. Shao, Y.; Xiao, Z.; Bi, C.; Yuan, Y.; Huang, J., Origin and elimination of photocurrent hysteresis by fullerene passivation in CH3NH3PbI3 planar heterojunction solar cells. *Nat Commun* **2014**, *5*, 5784.
21. Zhong, Y.; Hufnagel, M.; Thelakkat, M.; Li, C.; Huettner, S., Role of PCBM in the Suppression of Hysteresis in Perovskite Solar Cells. *Advanced Functional Materials* **2020**, *30*, 1908920.
22. Azmi, R.; Ugur, E.; Seitkhan, A.; Aljamaan, F.; Subbiah, A. S.; Liu, J.; Harrison, G. T.; Nugraha, M. I.; Eswaran, M. K.; Babics, M.; Chen, Y.; Xu, F.; Allen, T. G.; Rehman, A. u.;

Wang, C.-L.; Anthopoulos, T. D.; Schwingenschlögl, U.; De Bastiani, M.; Aydin, E.; De Wolf, S., Damp heat-stable perovskite solar cells with tailored-dimensionality 2D/3D heterojunctions. *Science* **2022**, *376* (6588), 73-77.
23. Chen, H.; Maxwell, A.; Li, C.; Teale, S.; Chen, B.; Zhu, T.; Ugur, E.; Harrison, G.; Grater, L.; Wang, J.; Wang, Z.; Zeng, L.; Park, S. M.; Chen, L.; Serles, P.; Awni, R. A.; Subedi, B.; Zheng, X.; Xiao, C.; Podraza, N. J.; Filleter, T.; Liu, C.; Yang, Y.; Luther, J. M.; De Wolf, S.; Kanatzidis, M. G.; Yan, Y.; Sargent, E. H., Regulating surface potential maximizes voltage in all-perovskite tandems. *Nature* **2023**, *613* (7945), 676-681.
24. Warby, J.; Zu, F.; Zeiske, S.; Gutierrez-Partida, E.; Frohloff, L.; Kahmann, S.; Frohna, K.; Mosconi, E.; Radicchi, E.; Lang, F.; Shah, S.; Peña-Camargo, F.; Hempel, H.; Unold, T.; Koch, N.; Armin, A.; De Angelis, F.; Stranks, S. D.; Neher, D.; Stolterfoht, M., Understanding Performance Limiting Interfacial Recombination in pin Perovskite Solar Cells. *Advanced Energy Materials* **2022**, *12*, 2103567 .
25. Li, X.; Zhang, W.; Guo, X.; Lu, C.; Wei, J.; Fang, J., Constructing heterojunctions by surface sulfidation for efficient inverted perovskite solar cells. *Science* **2022**, *375* (6579), 434-437.
26. Li, Z.; Li, B.; Wu, X.; Sheppard, S. A.; Zhang, S.; Gao, D.; Long, N. J.; Zhu, Z., Organometallic-functionalized interfaces for highly efficient inverted perovskite solar cells. *Science* **2022**, *376* (6591), 416-420.
27. Degani, M.; An, Q.; Albaladejo-Siguan, M.; Hofstetter, Y. J.; Cho, C.; Paulus, F.; Grancini, G.; Vaynzof, Y., 23.7% Efficient inverted perovskite solar cells by dual interfacial modification. *Science advances* **2021**, *7* (49), eabj7930.
28. Chen, C.; Liang, J.; Zhang, J.; Liu, X.; Yin, X.; Cui, H.; Wang, H.; Wang, C.; Li, Z.; Gong, J.; Lin, Q.; Ke, W.; Tao, C.; Da, B.; Ding, Z.; Xiao, X.; Fang, G., Interfacial engineering of a thiophene-based 2D/3D perovskite heterojunction for efficient and stable inverted wide-bandgap perovskite solar cells. *Nano Energy* **2021**, *90*, 106608.
29. Hsiao, K.-C.; Jao, M.-H.; Li, B.-T.; Lin, T.-H.; Liao, S. H.-C.; Wu, M.-C.; Su, W.-F., Enhancing Efficiency and Stability of Hot Casting p–i–n Perovskite Solar Cell via Dipolar Ion Passivation. *ACS Applied Energy Materials* **2019**, *2* (7), 4821-4832.
30. Lai, H.; Luo, J.; Zwirner, Y.; Olthof, S.; Wieczorek, A.; Ye, F.; Jeangros, Q.; Yin, X.; Akhundova, F.; Ma, T.; He, R.; Kothandaraman, R. K.; Chin, X.; Gilshtein, E.; Müller, A.; Wang, C.; Thiesbrummel, J.; Siol, S.; Prieto, J. M.; Unold, T.; Stolterfoht, M.; Chen, C.; Tiwari, A. N.; Zhao, D.; Fu, F., High-Performance Flexible All-Perovskite Tandem Solar Cells with Reduced VOC-Deficit in Wide-Bandgap Subcell. *Advanced Energy Materials* **2022**, *12* (45), 2202438.
31. Wang, C.; Shao, W.; Liang, J.; Chen, C.; Hu, X.; Cui, H.; Liu, C.; Fang, G.; Tao, C., Suppressing Phase Segregation in Wide Bandgap Perovskites for Monolithic Perovskite/Organic Tandem Solar Cells with Reduced Voltage Loss. *Small* **2022**, *18* (49), 2204081.
32. Zhang, X.; Qiu, W.; Song, W.; Hawash, Z.; Wang, Y.; Pradhan, B.; Zhang, Y.; Naumenko, D.; Amenitsch, H.; Moons, E.; Merckx, T.; Aguirre, A.; Abdulraheem, Y.; Aernouts, T.; Zhan, Y.; Kuang, Y.; Hofkens, J.; Poortmans, J., An Integrated Bulk and Surface Modification Strategy for Gas-Quenched Inverted Perovskite Solar Cells with Efficiencies Exceeding 22%. *Solar RRL* **2022**, *6*, 2200053.
33. Phung, N.; Verheijen, M.; Todinova, A.; Datta, K.; Verhage, M.; Al-Ashouri, A.; Kobler, H.; Li, X.; Abate, A.; Albrecht, S.; Creatore, M., Enhanced Self-Assembled Monolayer Surface Coverage by ALD NiO in p-i-n Perovskite Solar Cells. *ACS Appl Mater Interfaces* **2022**, *14* (1), 2166-2176.

34. Rakocevic, L.; Ernst, F.; Yimga, N. T.; Vashishtha, S.; Aernouts, T.; Heumueller, T.; Brabec, C. J.; Gehlhaar, R.; Poortmans, J., Reliable Performance Comparison of Perovskite Solar Cells Using Optimized Maximum Power Point Tracking. *Solar RRL* **2019**, *3*, 1800287.
35. Khenkin, M. V.; Katz, E. A.; Abate, A.; Bardizza, G.; Berry, J. J.; Brabec, C.; Brunetti, F.; Bulović, V.; Burlingame, Q.; Di Carlo, A.; Cheacharoen, R.; Cheng, Y.-B.; Colsmann, A.; Cros, S.; Domanski, K.; Dusza, M.; Fell, C. J.; Forrest, S. R.; Galagan, Y.; Di Girolamo, D.; Grätzel, M.; Hagfeldt, A.; von Hauff, E.; Hoppe, H.; Kettle, J.; Köbler, H.; Leite, M. S.; Liu, S.; Loo, Y.-L.; Luther, J. M.; Ma, C.-Q.; Madsen, M.; Manceau, M.; Matheron, M.; McGehee, M.; Meitzner, R.; Nazeeruddin, M. K.; Nogueira, A. F.; Odabaşı, Ç.; Osherov, A.; Park, N.-G.; Reese, M. O.; De Rossi, F.; Saliba, M.; Schubert, U. S.; Snaith, H. J.; Stranks, S. D.; Tress, W.; Troshin, P. A.; Turkovic, V.; Veenstra, S.; Visoly-Fisher, I.; Walsh, A.; Watson, T.; Xie, H.; Yıldırım, R.; Zakeeruddin, S. M.; Zhu, K.; Lira-Cantu, M., Consensus statement for stability assessment and reporting for perovskite photovoltaics based on ISOS procedures. *Nature Energy* **2020**, *5* (1), 35-49.
36. Xiao, K.; Lin, R.; Han, Q.; Hou, Y.; Qin, Z.; Nguyen, H. T.; Wen, J.; Wei, M.; Yeddu, V.; Saidaminov, M. I.; Gao, Y.; Luo, X.; Wang, Y.; Gao, H.; Zhang, C.; Xu, J.; Zhu, J.; Sargent, E. H.; Tan, H., All-perovskite tandem solar cells with 24.2% certified efficiency and area over 1 cm^2 using surface-anchoring zwitterionic antioxidant. *Nature Energy* **2020**, *5* (11), 870-880.
37. Boyd, C. C.; Cheacharoen, R.; Bush, K. A.; Prasanna, R.; Leijtens, T.; McGehee, M. D., Barrier Design to Prevent Metal-Induced Degradation and Improve Thermal Stability in Perovskite Solar Cells. *ACS Energy Letters* **2018**, *3* (7), 1772-1778.
38. Song, W.; Aernouts, T., Novel test scenarios needed to validate outdoor stability of perovskite solar cells. *Journal of Physics: Energy* **2020**, *2*, 021003 .
39. Wu, W.-Q.; Yang, Z.; Rudd, P. N.; Shao, Y.; Dai, X.; Wei, H.; Zhao, J.; Fang, Y.; Wang, Q.; Liu, Y.; Deng, Y.; Xiao, X.; Feng, Y.; Huang, J., Bilateral alkylamine for suppressing charge recombination and improving stability in blade-coated perovskite solar cells. *Science advances* **2019**, *5* (3), eaav8925.
40. Yang, S.; Chen, S.; Mosconi, E.; Fang, Y.; Xiao, X.; Wang, C.; Zhou, Y.; Yu, Z.; Zhao, J.; Gao, Y.; De Angelis, F.; Huang, J., Stabilizing halide perovskite surfaces for solar cell operation with wide-bandgap lead oxysalts. *Science* **2019**, *365* (6452), 473-478.
41. Meng, L.; Sun, C.; Wang, R.; Huang, W.; Zhao, Z.; Sun, P.; Huang, T.; Xue, J.; Lee, J. W.; Zhu, C.; Huang, Y.; Li, Y.; Yang, Y., Tailored Phase Conversion under Conjugated Polymer Enables Thermally Stable Perovskite Solar Cells with Efficiency Exceeding 21%. *Journal of the American Chemical Society* **2018**, *140* (49), 17255-17262.
42. Shockley, W.; Queisser, H. J., Detailed Balance Limit of Efficiency of p-n Junction Solar Cells. *Journal of Applied Physics* **1961**, *32* (3), 510-519.
43. Zhou, N.; Shen, Y.; Zhang, Y.; Xu, Z.; Zheng, G.; Li, L.; Chen, Q.; Zhou, H., CsI Pre-Intercalation in the Inorganic Framework for Efficient and Stable $FA_{1-x}Cs_xPbI_3(Cl)$ Perovskite Solar Cells. *Small* **2017**, *13*, 1700484.
44. Zhou, Q.; Liang, L.; Hu, J.; Cao, B.; Yang, L.; Wu, T.; Li, X.; Zhang, B.; Gao, P., High-Performance Perovskite Solar Cells with Enhanced Environmental Stability Based on a $(p\text{-}FC_6H_4C_2H_4NH_3)_2[PbI_4]$ Capping Layer. *Advanced Energy Materials* **2019**, *9* (12).
45. Thote, A.; Jeon, I.; Lee, J.-W.; Seo, S.; Lin, H.-S.; Yang, Y.; Daiguji, H.; Maruyama, S.; Matsuo, Y. Stable and Reproducible 2D/3D Formamidinium–Lead–Iodide Perovskite Solar Cells. *ACS Appl. Energy Mater.* 2019, *2*, 2486-2493.
46. Zhou, Z.; Pang, S.; Liu, Z.; Xu, H.; Cui, G., Interface engineering for high-performance perovskite hybrid solar cells. *Journal of Materials Chemistry A* **2015**, *3* (38), 19205-19217.
47. Yang, Z.; Dou, J.; Wang, M., Interface Engineering in n-i-p Metal Halide Perovskite Solar Cells. *Solar RRL* **2018**, *2*, 1800177.

48. Al-Ashouri, A.; Magomedov, A.; Roß, M.; Jošt, M.; Talaikis, M.; Chistiakova, G.; Bertram, T.; Márquez, J. A.; Köhnen, E.; Kasparavičius, E.; Levcenco, S.; Gil-Escrig, L.; Hages, C. J.; Schlatmann, R.; Rech, B.; Malinauskas, T.; Unold, T.; Kaufmann, C. A.; Korte, L.; Niaura, G.; Getautis, V.; Albrecht, S., Conformal monolayer contacts with lossless interfaces for perovskite single junction and monolithic tandem solar cells. *Energy & Environmental Science* **2019**, *12* (11), 3356-3369.
49. Wang, Q.; Chueh, C. C.; Zhao, T.; Cheng, J.; Eslamian, M.; Choy, W. C. H.; Jen, A. K., Effects of Self-Assembled Monolayer Modification of Nickel Oxide Nanoparticles Layer on the Performance and Application of Inverted Perovskite Solar Cells. *ChemSusChem* **2017**, *10* (19), 3794-3803.
50. Al-Ashouri, A.; Köhnen, E.; Li, B.; Magomedov, A.; Hempel, H.; Caprioglio, P.; Márquez, J. A.; Morales Vilches, A. B.; Kasparavicius, E.; Smith, J. A.; Phung, N.; Menzel, D.; Grischek, M.; Kegelmann, L.; Skroblin, D.; Gollwitzer, C.; Malinauskas, T.; Jošt, M.; Matič, G.; Rech, B.; Schlatmann, R.; Topič, M.; Korte, L.; Abate, A.; Stannowski, B.; Neher, D.; Stolterfoht, M.; Unold, T.; Getautis, V.; Albrecht, S., Monolithic perovskite/silicon tandem solar cell with >29% efficiency by enhanced hole extraction. *Science* **2020**, *370* (6522), 1300-1309.
51. Bai, Y.; Chen, H.; Xiao, S.; Xue, Q.; Zhang, T.; Zhu, Z.; Li, Q.; Hu, C.; Yang, Y.; Hu, Z.; Huang, F.; Wong, K. S.; Yip, H.-L.; Yang, S., Effects of a Molecular Monolayer Modification of NiO Nanocrystal Layer Surfaces on Perovskite Crystallization and Interface Contact toward Faster Hole Extraction and Higher Photovoltaic Performance. *Advanced Functional Materials* **2016**, *26* (17), 2950-2958.
52. Mann, D. S.; Patil, P.; Kwon, S.-N.; Na, S.-I., Enhanced performance of p-i-n perovskite solar cell via defect passivation of nickel oxide/perovskite interface with self-assembled monolayer. *Applied Surface Science* **2021**, *560*, 149973.
53. Guo, Y.; Apergi, S.; Li, N.; Chen, M.; Yin, C.; Yuan, Z.; Gao, F.; Xie, F.; Brocks, G.; Tao, S.; Zhao, N., Phenylalkylammonium passivation enables perovskite light emitting diodes with record high-radiance operational lifetime: the chain length matters. *Nat Commun* **2021**, *12* (1), 644.
54. Apergi, S.; Brocks, G.; Tao, S., Tuning the electronic levels of NiO with alkali halides surface modifiers for perovskite solar cells. *Physical Review Materials* **2020**, *4*, 085403.
55. Lee, J. W.; Dai, Z.; Han, T. H.; Choi, C.; Chang, S. Y.; Lee, S. J.; De Marco, N.; Zhao, H.; Sun, P.; Huang, Y.; Yang, Y., 2D perovskite stabilized phase-pure formamidinium perovskite solar cells. *Nat Commun* **2018**, *9* (1), 3021.
56. Chen, C.; Song, Z.; Xiao, C.; Awni, R. A.; Yao, C.; Shrestha, N.; Li, C.; Bista, S. S.; Zhang, Y.; Chen, L.; Ellingson, R. J.; Jiang, C.-S.; Al-Jassim, M.; Fang, G.; Yan, Y., Arylammonium-Assisted Reduction of the Open-Circuit Voltage Deficit in Wide-Bandgap Perovskite Solar Cells: The Role of Suppressed Ion Migration. *ACS Energy Letters* **2020**, *5* (8), 2560-2568.
57. Bai, Y.; Xiao, S.; Hu, C.; Zhang, T.; Meng, X.; Lin, H.; Yang, Y.; Yang, S., Dimensional Engineering of a Graded 3D-2D Halide Perovskite Interface Enables Ultrahigh V_{oc} Enhanced Stability in the p-i-n Photovoltaics. *Advanced Energy Materials* **2017**, *7*, 1701038.
58. Kim, M.; Kim, G.-H.; Lee, T. K.; Choi, I. W.; Choi, H. W.; Jo, Y.; Yoon, Y. J.; Kim, J. W.; Lee, J.; Huh, D.; Lee, H.; Kwak, S. K.; Kim, J. Y.; Kim, D. S., Methylammonium Chloride Induces Intermediate Phase Stabilization for Efficient Perovskite Solar Cells. *Joule* **2019**, *3* (9), 2179-2192.
59. Jiang, Q.; Zhao, Y.; Zhang, X.; Yang, X.; Chen, Y.; Chu, Z.; Ye, Q.; Li, X.; Yin, Z.; You, J., Surface passivation of perovskite film for efficient solar cells. *Nature Photonics* **2019**, *13* (7), 460-466.